

# APPLICATION OF LUCAS-KANADE DENSE FLOW FOR TERRAIN MOTION IN LANDSLIDE MONITORING APPLICATION

V. Yordanov<sup>1,\*</sup>, X. Q. Truong<sup>2</sup>, M. Corti<sup>1</sup>, L. Longoni<sup>1</sup>, M. A. Brovelli<sup>1,3</sup>

<sup>1</sup> Politecnico di Milano, Department of Civil and Environmental Engineering, Piazza Leonardo da Vinci 32, Milan, Italy  
- (vasil.yordanov, monica.corti, laura.longoni, maria.brovelli)@polimi.it

<sup>2</sup> Hanoi University of Natural Resources and Environment, Information Technology Faculty,  
41A Phu Dien Road, Phu Dien, North-Tu Liem district, Hanoi, Vietnam - txquang@hunre.edu.vn

<sup>3</sup> Istituto per il Rilevamento Elettromagnetico dell'Ambiente, CNR-IREA, via Bassini 15, 20133 Milano

## Commission II, WG II/1

**KEY WORDS:** Landslide, Simulator, Optical flow, Computer vision, Displacements, Magnitude

### ABSTRACT:

Landslides are natural hazards that can cause severe damage and loss of life. Optical cameras are a low-cost and high-resolution alternative among many monitoring systems, as their size and capabilities can vary, allowing for flexible implementation and location. Computer vision is a branch of artificial intelligence that can analyze and understand optical images, using techniques such as optical flow, image correlation and machine learning. The application of such techniques can estimate the motion vectors, displacement fields, providing valuable information for landslide detection, monitoring and prediction. However, computer vision also faces some challenges such as illumination changes, occlusions, image quality, and computational complexity. In this work, a computer vision approach based on Lucas-Kanade optical dense flow was applied to estimate the motion vectors between consecutive images obtained during landslide simulations in a laboratory environment. The approach is applied to two experiments that vary in their illumination and setup parameters to test its applicability. We also discuss the application of this methodology to images from Sentinel-2 satellite optical sensors for landslide monitoring in real-world scenarios.

## 1. INTRODUCTION

Landslides are widespread natural hazards that can cause significant damage to infrastructure, property, and human life. Therefore, it is essential to monitor landslide-prone areas to detect early warning signs and mitigate the risk of landslides. However, traditional landslide monitoring techniques involve the use of sensors and instruments, which can be expensive and challenging to maintain in remote or inaccessible areas (Casagli et al., 2023, Lissak et al., 2020).

Optical cameras offer a promising alternative for monitoring landslides due to their ease of installation, low cost, and high-resolution imaging capabilities. Moreover, they can capture images of the slope before, during, and after a landslide event, providing valuable data for analysis and modelling (Auflič et al., 2023). Several studies have applied optical cameras for landslide detection, monitoring and prediction using various methods such as photogrammetry, image correlation, optical flow and machine learning (Hermle et al., 2021).

Computer vision is a branch of artificial intelligence that deals with the analysis and understanding of images/videos and has been increasingly applied for landslide monitoring, as it can provide high-resolution and near-real-time information on the slope dynamics and deformation (Casagli et al., 2023). Some of the computer vision techniques that have been used for landslide monitoring include optical flow, image correlation, image differencing, machine learning (Muhammad et al., 2022). These techniques can estimate the motion vectors, displacement

fields, similarity indices, and classification labels of the images captured by optical cameras. Computer vision can also complement other remote sensing techniques such as InSAR and LiDAR, by overcoming some of their limitations as line-of-sight constraints, temporal decorrelation, and atmospheric effects (Muhammad et al., 2022). However, there are some challenges such as sensitivity to illumination changes, occlusions, image quality, and computational complexity (Hermle et al., 2022). There is still room for improvement and innovation in developing landslide monitoring techniques using images from optical sensors (Mazzanti et al., 2020, Yordanov et al., 2023). Therefore, computer vision requires careful calibration, validation, and integration with other methods to achieve reliable and robust results for landslide monitoring.

In this work, we adopt a computer vision approach based on Lucas-Kanade implementation of optical dense flow (Lucas et al., 1981) for estimating the motion vectors between consecutive images obtained during landslide simulations in a laboratory environment. By estimating the magnitude and direction of the movement this technique allows one to track the movement of terrain and detect any signs of slope instability or deformation. We also discuss the advantages and challenges of using the proposed methodology applied to images from satellite optical sensors onboard Sentinel-2 for landslide monitoring in real-world scenarios. Our work efforts are to contribute to improving our understanding of landslide mechanisms and behaviour, enhancing early warning systems, and facilitating effective decision-making in landslide-prone areas.

\* Corresponding author

## 2. SETUP

### 2.1 Landslide simulator

Physical landslide simulators that are used in a controlled laboratory environment are allowing scholars to mimic real-world slope conditions and simulate various landslide scenarios by applying various conditions. In particular, these experiments represent a good strategy to better analyse the influence of the different triggering and predisposing factors to land sliding, such as precipitation intensity and slope. In this study, the authors considered two rainfall-induced landslide simulations performed with a custom-built simulator where the inclinable surface hosting the material for tests has a size of 2 x 0.8 meters and can be inclined up to 45° (Figure 1). A geogrid installed on the bottom of the flume ensures a grip between the landslide material and the inclined surface. The structure includes a system of six sprinklers capable of simulating rainfalls of different intensities up to the maximum of 20.6 mm/h per nozzle. The sprinklers are disposed on the top of the structure at a height of 0.6 m along two parallel rows, set in order to supply rainfall spray homogeneously. Their discharge is controlled through a pressure reduction valve and rainfall intensity can be estimated through the pressure-discharge characteristic curve provided by the manufacturer. Please refer to (Ivanov et al., 2020, Longoni et al., 2022) for the full description of the landslide simulator.

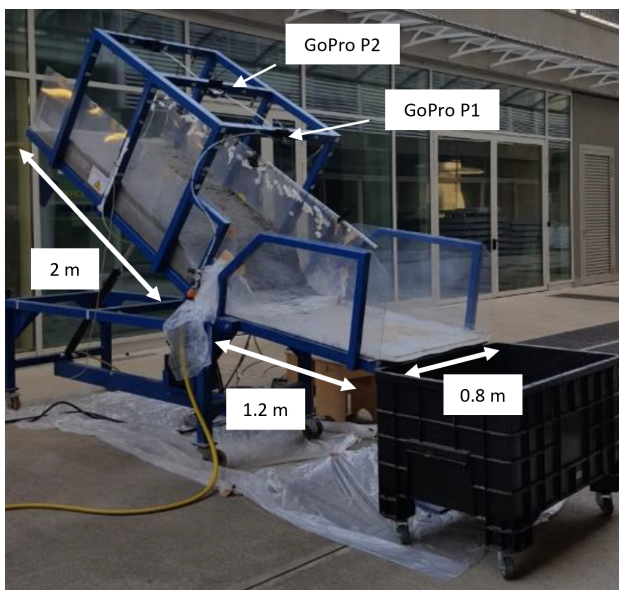


Figure 1. Landslide simulator setup.

### 2.2 Experiments

As in (Ivanov et al., 2020, Ivanov et al., 2021, Longoni et al., 2022, Panzeri et al., 2022), the landslide bodies of the present work experiments were both composed of homogeneous medium sand ( $d_{50} = 0.35$  mm, uniformity coefficient  $C_u = 1.75$ , internal friction  $\phi = 34^\circ$ ). The sand was disposed in the flume in three steps, laying and compacting three subsequent sand layers in order to achieve a uniform compaction for a total thickness of 15 cm. The degree of sand compaction was derived from a relationship between the volume of each layer and the mass of the material.

The final porosity of both the landslide bodies was then around 50%. In addition, the initial soil moisture content was set to

a predefined value at the beginning of the experiments. In the second experiment, the volumetric water content (VWC) was monitored with a time step of 1 minute by a time-domain reflectometer (TDR) inserted within the soil at mid-slope. Three tensiometers were also employed for the evaluation of suction and they were located at the top, in the middle and at the bottom of the slope. All the probes were placed at mid-depth of the soil, in order to minimize the effect of boundaries.

In order to validate the Lucas-Kanade optical dense flow method, the optical cameras and the abovementioned traditional monitoring system were coupled with consecutive electrical resistivity tomography (ERT) surveys. The ERT gave continuous information on water saturation throughout the whole duration of the tests. Moreover, the ERT survey is capable of detecting seepage zones and the development of failure. The ERT procedure, its configuration and the data post-processing are described in (Hojat et al., 2019). After the terrain and the monitoring system had been settled, the upper platform was lifted and rainfall was initiated. In the current work, images from two experiments were used featuring a similar setting with the exception of rainfall simulation. In the first experiment (denoted Test 1), rainfall was simulated as a constant for the first 10 minutes, then it was paused for 10 minutes and finally it was again constant with a different intensity until failure. In the second experiment (Test 2), rainfall was constant and continuous all over the experiment, but it was concentrated only in the upper part of the slope. The summary of the two experiment settings is in Table 1.

Test	I [mm/h]	Vw [l]	n [-]	$\theta$ [-]	Sr [-]	$\alpha$ [°]	$k_s$ [m/s]	$t_f$ [min]
1	48.5 and 82	0.056	0.50	0.10	0.20	35	5.2 E-04	44.5
2	72	0.040	0.51	0.11	0.22	35	5.6 E-04	21

Table 1. Experiment settings summary; I is rainfall intensity, Vw is volume of water, n is porosity,  $\theta$  is Volumetric Water Content, Sr is saturation degree,  $\alpha$  is slope,  $k_s$  is saturated hydraulic conductivity,  $t_f$  is time of failure. The two values of rainfall intensity of Test 1 are referred to the constant rainfall set before and after the pause of 10 minutes.

### 2.3 Cameras

Among various geophysical and traditional instruments, the simulator incorporates imaging tools to document experiments and apply remote sensing techniques. Specifically, this study utilizes GoPro action cams, namely Hero Session and Black 4, known for their ability to capture high-resolution photos and videos while remaining lightweight and robust (Scaioni et al., 2018). The GoPro Hero Session is a compact, waterproof action camera equipped with a 10-megapixel sensor, a 123° Field of View (FOV), and a fixed focal length of 16.8 mm. Similarly, the GoPro Hero Black 4 is also an action camera with a 12-megapixel sensor, a wide FOV of 118.2 degrees, and a fixed focal length of 15mm. Both cameras feature a time-lapse photo mode that allows for controlling the image acquisition time-step based on the experimental requirements. In the current experiments, the cameras were positioned differently in relation to the landslide body, specifically at two distinct points labelled as P1 and P2 (refer to Figure 1). In Test 1, only the GoPro Hero Session placed at P1 was used, providing an oblique view of the landslide body. The camera was set to take photos every 30 seconds. In the second experiment (Test 2), the Hero Black 4 was placed at P2, capturing a nadir view of the slope. In this case, the images were acquired at a much faster rate, every 2 seconds.

### 3. METHODOLOGY

#### 3.1 Preprocessing

Four preprocessing steps are needed before directly using the imagery.

**3.1.1 Camera calibration** - In order to correct the geometric and optical distortions caused by the wide camera lens (Figure 2a) a traditional camera calibration approach was implemented. A chessboard pattern was used as a reference object and multiple images from different viewpoints were captured. Then, through the OpenCV library (Bradski, 2000) the corners of the chessboard were detected to compute the camera matrix and the distortion coefficients. By having the intrinsic properties of the camera, such as focal length, optical center, and distortion level the captured images from the experiments were undistorted, and the results were rectified images (e.g., Figure 2b).

**3.1.2 Masking** - To focus the processing only on the landslide body itself, the images were masked with experiment-specific regions of interest. We cropped the images to the areas that contained the landslide area, which reduced the number of pixels and features that needed to be processed. This action further sped up the computation and saved memory.

**3.1.3 Ground Sampling Distance** - using the sensors' parameters and the distance between the landslide body and camera sensor it was possible to compute the GSD which represents the distance between two consecutive pixel centres measured on the ground, i.e. the spatial resolution of the image. The GSD was computed according to the following formula:

$$GSD = \frac{H \times S}{F \times I}, \quad (1)$$

where  $H$  is the height,  
 $S$  is the sensor size,  
 $F$  is the focal length,  
 $I$  is the image size.

However, it should be highlighted the fact that Formula 1 could be used directly in Test 2 (e.g., Figure 2c) as the camera was at nadir position P2. For the setup from Test 1, an additional step was needed to compute the resolution.

**3.1.4 Distance Gradient** - as the camera location in Test 1 was obliquely placed towards the landslide body, it was needed to estimate a distance gradient for the camera's sensor in relation to the landslide crown and toe. The resulting gradient (Figure 2d) was used in the previous Formula 1 to compute the apparent GSD along the slope.

#### 3.2 Optical dense flow

In this work, the Lucas-Kanade (LK) optical flow algorithm (Lucas et al., 1981) was employed for estimating displacement using time-series images from a landslide simulator. It is a classic technique in computer vision for estimating apparent motion between consecutive images or frames (Horn and Schunck, 1981). It is based on the assumption of local brightness constancy, which states that the intensity of a pixel should remain constant as it moves within a small neighbourhood over time.

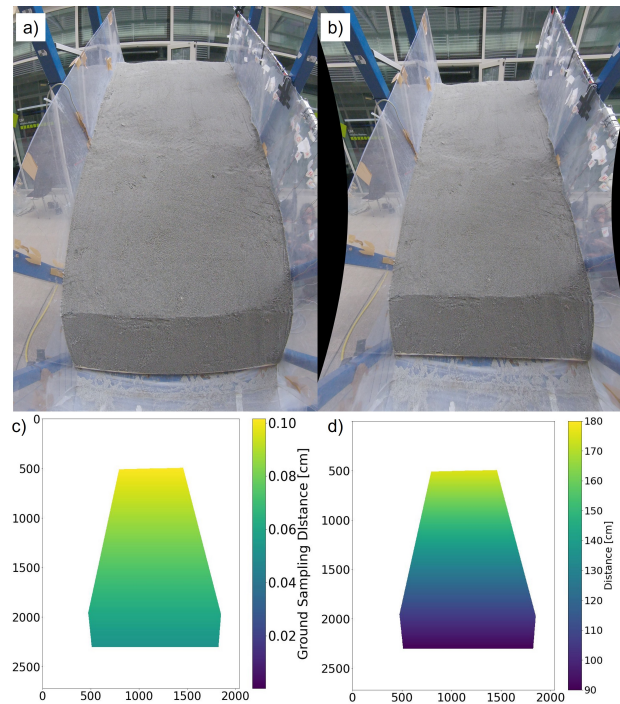


Figure 2. a) Raw image, b) Undistorted image, c) Masked GSD and d) Masked distance gradient.

The method assumes that the flow is constant in a local neighbourhood of the pixel under consideration and solves the optical flow equation for all the pixels in that neighbourhood, by the least squares criterion. By solving the system of equations for each window, the algorithm computes a dense optical flow field, providing a detailed representation of the apparent motion across the entire image. To optimize computational efficiency, the LK algorithm incorporates an inverse pyramid strategy known as a coarse-to-fine window search. This strategy involves performing the optical flow estimation process iteratively, starting with a downsampled version of the image and gradually refining the estimation at higher resolution levels. By using this pyramid approach, the algorithm progressively refines the optical flow estimation and reduces the computational burden associated with dense estimation on high-resolution images.

The LK algorithm has been widely used in classical computer vision applications (Kollnig et al., 1994, Pantilie et al., 2010) and in the Earth Observation domain (Vogel et al., 2012, Lenzano et al., 2018). Its effectiveness in tracking small, dense image motion over time makes it particularly well-suited for analysing subtle changes in the landscape, such as those indicative of slope instability or deformation.

The method implementation was using the Scikit-image library (Walt et al., 2014), which provided us with the necessary tools to analyse the time-series images from the landslide simulator. By leveraging the functionalities of the library, we were able to estimate the displacement of some selected points of interest (POIs) over time (e.g., Figure 3), enabling us to track and understand the movement patterns within the simulated landslide. In the current setups, those locations are selected in areas of crack formations.

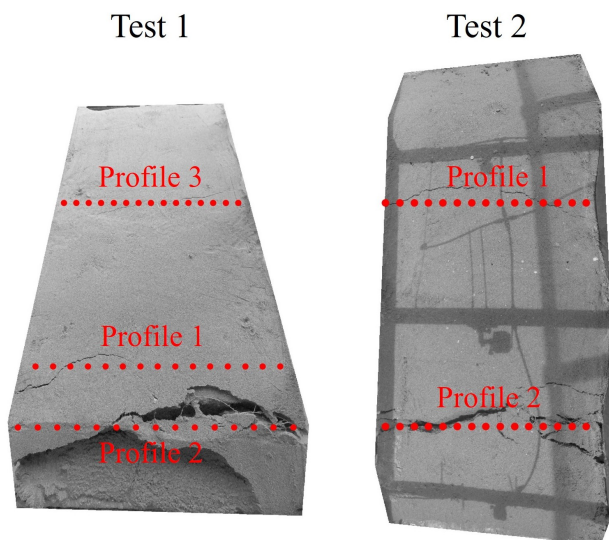


Figure 3. Example of points of interest chosen for sampling strategy to track and measure displacement over time.

### 3.3 Comparison with a traditional monitoring system

In order to evaluate the performance of the proposed method, a comparison was carried out with the data gained from the monitoring system of Test 2. The traditional monitoring system installed on the landslide simulator was chosen based on the typical characteristic of shallow landslides to be induced by rainfall (Baum et al., 2010), and therefore by the propagation of the wetting front propagation from the soil surface. As mentioned in Section 2.2, the authors considered 4 punctual measurements, performed by one TDR probe and by three tensiometers, and consecutive longitudinal ERT profiles. The TDR measures the Volumetric Water Content [%], which is related to soil saturation (for the present test setting,  $VWC = 40\%$  corresponds almost to complete saturation). On the other hand, tensiometers measure pressure [kPa] and temperature [°C]. In order to evaluate soil suction, porous heads full of water were installed on the tensiometers, therefore the pressure measured by the tensiometers was the negative pressure of water flowing out of the porous heads and soil saturation is reached when the measured value is zero (Kandelous et al., 2015, Wu et al., 2015, Panzeri et al., 2022). As regards the ERT profiles, the measurements taken every 3-4 minutes show the variation of soil resistivity, which is related to the increase/decrease of water content (Hojat et al., 2019, Ivanov et al., 2020). When failure occurred, starting from the toe of the slope, either the electrodes or the bottom tensiometer resulted exposed and their recording ended.

### 3.4 Proof-of-concept application

To validate our approach to a realistic scenario, we evaluated it on optical satellite images, especially from the ESA's Sentinel-2 mission. The adopted landslide case study is the Ruinon landslide in Northern Italy, which was active in the period 2019-2021 and thoroughly studied by using ground-, air- and spaceborne means (Del Ventisette et al., 2012, Carlà et al., 2021, Amici et al., 2022, Yordanov et al., 2023). This application offers a more challenging and practical setting, as Sentinel-2 (SE2) images have a much lower spatial resolution (10 m/pix) compared to the submillimetre level of the simulator setup. Moreover, external factors such as cloud cover, vegetation seasonality and uncontrolled image acquisition can

introduce more variability and complexity in the data. This case study follows the already defined SE2 yearly application scheme used by (Amici et al., 2022) for the application of local Maximum Cross-Correlation (MCC) analysis, i.e. the applicability of LK dense flow for displacement estimation was tested on one image per year for the period 2015 to 2020.

## 4. RESULTS

The initial implementations of the approach for the surveys depicted very promising results, in terms of accuracy and robustness. Moreover, the approach managed to highlight areas that tend to move at a millimetre level before actually a formed crack. Further, tuning of the optical flow parameters was needed to result in a more precise outcome which will allow the detection of the collapse signatures. The findings from each experiment are discussed below.

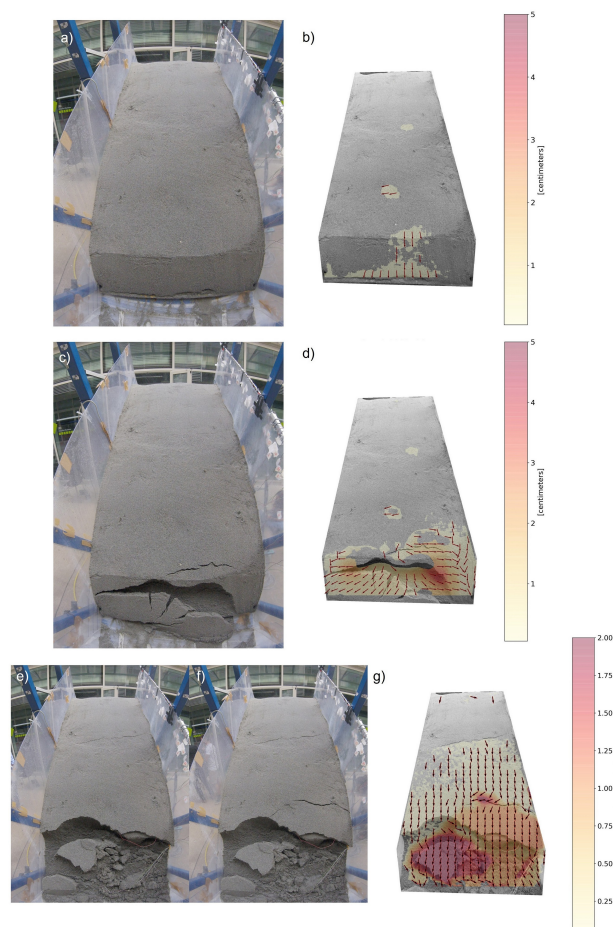


Figure 4. a) and c) Images at epochs 87 and 89. b) and d) Magnitude and vector field from the estimated displacements at epochs 87 and 89. e) and f) Images at epochs 103 and 104. g) Magnitude and vector field from the estimated displacement between epochs 103 and 104.

### 4.1 Displacement estimation from Lucas-Kande dense flow

**4.1.1 Test 1** The overall setup of the experiment, in terms of constant and diffused light conditions without any strong shadows, allowed easy parameter tuning for the optical flow computation, where the final results were obtained by using a

searching  $radius = 16$  pix and  $nuw\_wrap = 2$ . The higher windows search values were needed due to the higher time-step between two images and the relatively lower sensor resolution of the GoPro Hero Session camera. Overall, few false displacements were mapped, with the exception of two mid-body round clusters that were detected (e.g., Figure 4b). Upon visual inspection, it was determined that those areas were the result of sprinkle drips that were oversaturating them and locally displacing sand particles.

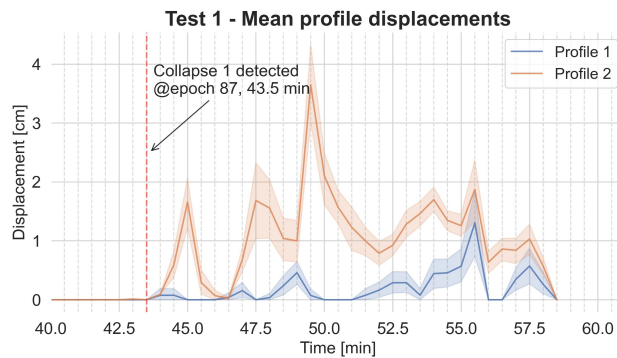


Figure 5. Averaged profile sampled values with highlighted the first collapse.

In Test 1, the first crack was formed at the toe of the landslide body (Profile 2 at Figure 3). Unfortunately, during the current setup, there were no additional tools that could determine the exact time of the collapse. However, as pointed out in Table 1 and upon visual evaluation, the crack appeared between 44 and 44.5 min (epoch 88 and 89, Figure 4). From the optical flow computation and the results of displacement magnitudes and vectors computation, the first signals of slope collapse can be noted at 43.5 mins (epoch 87) both from the magnitude field (Figure 4b) and the summary of the extracted values (Figure 5). The maximum displacement was computed at 5.47 cm on Profile 2 at 49.5 min.

**4.1.2 Test 2** In terms of parameter tuning, it was decided to keep the same window size and number of wraps as in the first setup. However, except for the processing parameters, the overall test setup differed in many aspects from Test 1. Starting from the camera, GoPro Hero Black 4 exhibited better sensor parameters compared to Hero Session, therefore the higher GSD = 0.036 cm. Moreover, due to the nadir position the GSD was constant over the whole landslide body. Moreover, the higher GSD and higher image acquisition step of 2 seconds allowed much better overall simulation documentation and greater detail when optical flow estimation was applied. In contrast to the diffused lighting conditions during the first experiment, during Test 2 the conditions were different with a bright sun casting strong shadows on the landslide body, resulting in varying pixel intensity on the landslide body. If the camera timelapse settings had been kept as in the previous iteration (30 secs) and considering the duration of around 1 hour in total for the whole experiment, this would have yielded false results, as the casted shadows would have eventually moved from their initial positions. However, the faster image acquisition in the current setup mitigated this issue as in the span of 2 seconds the shadows could be considered static and there was no rapid pixel intensity change. Nevertheless, the oblique sunlight raised another issue - the water drops from the sprinkler systems were visible and actually appeared as moving between two epochs. To reduce the effect of the resulting noise, an additional processing

filter was applied to the vector field to disregard any apparent motions if they were not in the slope-moving direction (i.e. towards the local south). However, it was further observed that a consistent spatial field in terms of magnitude and movement direction was a signal for a true displacement.

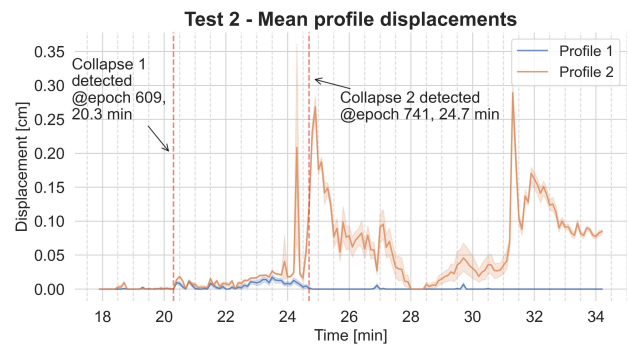


Figure 6. Averaged profile sampled values with highlighted the first and second collapses.

Overall, two crack formations of the landslide body appeared during the experiment, where the first one was in the upper part (Figure 3 Test 2, Profile 1) and the subsequent one collapsed towards the toe (Figure 3 Test 2, Profile 2). By overlaying the displacements from both of the profiles (Figure 6 we were able to clearly define the timing of the first and second collapse. Collapse 1 was determined at epoch 609 (20.3 min), while the second one was at epoch 741 (24.7 min). Everything prior to those timings was considered as erroneous noise mainly due to the fact that the estimated movements were not consistent in both profiles. The following higher displacements rates in Profile 2 are mainly due to the continuous slide of the detached sand block. However, the spike before the crack formation can be assumed as an indication of the failure development. Similarly, Profile 1 exhibited increased magnitude rates until the complete collapse in that area and no further movement was detected. There is a notable difference between the displacement rates between Test 1 and Test 2, where for Test 2 much lower magnitudes were estimated at each epoch. This is a direct consequence of the higher image acquisition rate.

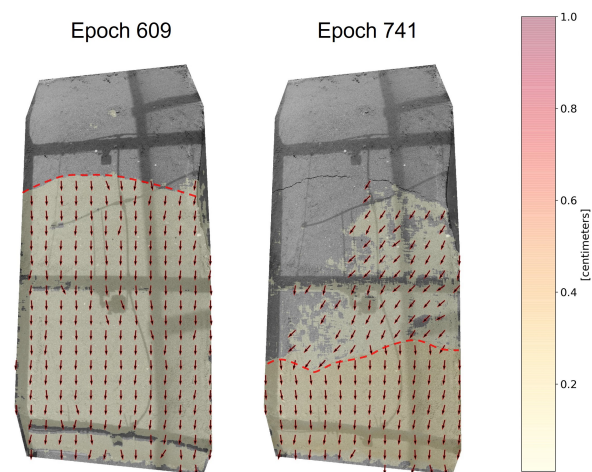


Figure 7. Magnitude and vector fields at the crack formation moments. The red dash line highlights the formed cracks.

Side-by-side comparison of the displacement plots with the

magnitude and vector fields (Figure 7) further confirms the initial moving time. In both of the epochs are present consistent fields with a moving direction downslope and their upper bounds are clearly defining the crack locations.

**4.1.3 Sentinel-2 yearly application** Except for the application of the proposed approach on a landslide simulator in a controlled environment, we have applied the Lukas-Kanade dense optical flow using Sentinel-2 multispectral images for landslide monitoring in the period 2015-2020. Obviously, such implementation restricts the usable images as the area of interest is in a mountainous area with frequent and complete cloud cover, which in certain periods can lead to one usable image per month. However, another difference with the laboratory setup is that the real application offers a higher variety of features with variable intensities that should ensure better feature detection and subsequent displacement field. As for the computation parameters of the optical flow they had to be adjusted accordingly to the available SE2 resolution of 10 m/pix, thus a searching window of 7 pixels was determined to be suitable for clipped imagery with a size of 119x108 pixels. The number of wraps was kept the same, two, as the experimental setups.

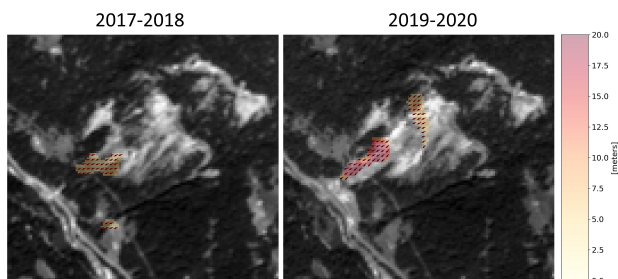


Figure 8. Magnitude and vector fields from the yearly analysis of Sentinel-2 images.

Overall, the results depict accurate estimated displacement fields and movement directions which are in line with the ones reported in previous studies (Amici et al., 2022). The estimated magnitudes range from a few meters to more than 20 meters between two acquisitions. The direction of the movement is also correctly estimated as South-West downhill direction. However, as a notable drawback of the current implementation, it could be pointed out that the images are acquired with a high temporal difference between them. Even though the landslide developed over a period of years, it had significant reactivations, particularly intensive in the summer months of each year. Therefore, such dynamic phenomena would lead to highly displaced features or those totally absent in a consecutive acquisition, which results in decorrelated areas in the estimated magnitude fields. Such an example can be noted in the 2019-2020 (Figure 8) image analysis where there is a significant gap between uphill and downhill fields. Different errors are noted in the period 2017-2018, where false positive displacements are computed for stable areas. This effect is due to the difference in the vegetation phase leading to inconsistent feature intensity. Therefore, it is suggested to apply the proposed approach with a balanced acquisition rate according to the expected displacements.

## 4.2 Validation

As fully described by (Ivanov et al., 2020) after the analysis of 20 similar downscaled landslide simulations, the failure of the

present work tests developed through the opening of a series of cracks from the surface of the sand body, induced by the propagation of the wetting front. In Table 1, the first crack opening times are reported. Commonly, failure starts from the toe of the slope and spread towards the top of the flume in a retrogressive way in this type of setting. In Test 2, the first crack occurred at mid-slope, and then failure propagation concentrated at the toe. According to this visual interpretation of the collapse, the monitoring system of Test 2 registered an increase in soil water saturation (Figure 9). The tensiometers, located in the three different sectors of the flume, recorded at different timing the increase of pore water pressure. As rainfall was concentrated in the upper part of the slope, the bottom tensiometer registered it later than the others. The first crack occurred when VWC was almost 30%, which corresponds to  $S_r = 60\%$ , and suction was about -0.7 kPa. These values stabilized until the occurrence of the complete collapse four minutes later. Cracks developing are also shown by the ERT profiles in Figure 9. After the end of the test, the simulator was rotated back to the horizontal position without stopping the rainfall for the complete saturation of the sand, which is again recorded by the instruments in Figure 9.

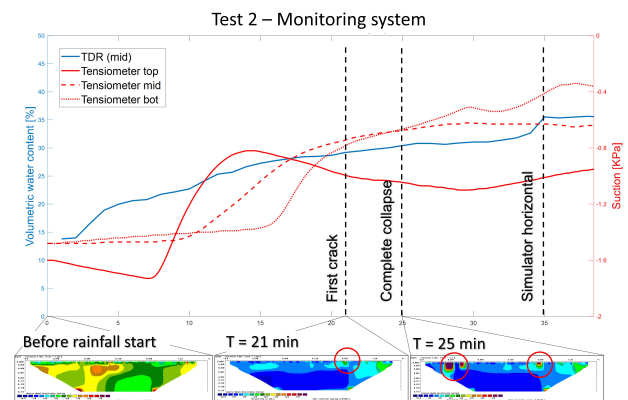


Figure 9. Traditional monitoring system results: volumetric water content registered by a TDR probe located at mid-slope, suction registered by three tensiometers located in the three slope sectors (top, middle, bottom of the slope) and ERT longitudinal profiles along the whole slope (upslope is on the right and downslope to the left of the profiles). The four probes record the increase of water content that drove the instability and ERT profiles show the developing of cracks from the sand surface inside the landslide body.

## 5. CONCLUSION

In this work, a computer vision approach based on optical dense flow for landslide monitoring using images from optical cameras was applied. The methodology was tested on two rainfall-induced landslide simulations performed in a laboratory environment, using portable action cameras, and on a real-world case study of the Ruinon landslide in Italy, using spaceborne multispectral images. The approach was able to estimate the motion vectors, displacement fields, and movement directions of the slope before, during, and after the landslide events. Further, the results from the simulator were compared with traditional monitoring systems such as volumetric water content and electrical resistivity tomography. We found that our approach can provide high-resolution and near-real-time information on slope dynamics and deformation, as well as detect early warning signs of slope failure.

We also discussed the advantages and challenges of using optical cameras and computer vision for landslide monitoring, such as the high-resolution imaging capabilities, sensitivity to illumination changes, occlusions and image quality. It can be concluded that the computer vision approach based on optical dense flow has several advantages over traditional landslide monitoring techniques that rely on sensors and instruments. First, it can capture images of the slope at high spatial and temporal resolutions, which can reveal subtle changes and movements that might otherwise go unnoticed. Secondly, it can estimate the motion vectors and displacement fields of the slope without requiring any prior knowledge or assumptions about the landslide geometry or mechanics. Third, it can provide near-real-time information on slope dynamics and deformation, which can be useful for early warning systems and decision-making. Our results from the laboratory experiments and the real-world case study demonstrate the potential and feasibility of our approach to be implemented for landslide monitoring. We were able to detect the crack formations and slope failures in both scenarios. In addition, good agreement was found between our results and the ones obtained from other traditional monitoring systems.

Naturally, further improvements are possible in the proposed methodology by addressing some of the limitations and challenges we encountered. More sophisticated image processing and filtering techniques can be applied to reduce the noise and artefacts caused by water drops, shadows, and vegetation. In addition, further testing can be carried out on real-world landslide monitoring cameras. Such computer vision requires careful calibration, validation, and integration with other methods to achieve reliable and robust results for landslide monitoring. However, the proposed approach can complement traditional monitoring systems by providing additional information on the slope surface and motion.

## 6. ACKNOWLEDGEMENTS

The authors gratefully acknowledge professor Hojat and professor Zanzi from Politecnico di Milano for their important contribution for the realization of the ERT profiles, Lorenzo Panzeri, Monica Papini and Michele Mondani for the landslide simulations, and Lorenzo Amici for the analysis-ready Sentinel-2 images.

This work is partially funded by the Italian Ministry of Foreign Affairs and International Cooperation within the project “Geoinformatics and Earth Observation for Landslide Monitoring” CUP D19C21000480001 (Italian side) and partially funded by the Ministry of Science and Technology of Vietnam (MOST) (Vietnamese side) by the Bilateral Scientific Research project between Vietnam and Italy, code: NDT/IT/21/14.

## REFERENCES

Amici, L., Yordanov, V., Oxoli, D., Truong, X. Q., Brovelli, M. A., 2022. Monitorin landslide displacements through maximum cross-correlation of satellite images. *The International Archives of the Photogrammetry, Remote Sensing and Spatial Information Sciences*, XLVIII-4/W1-2022, 27–34. <https://www.int-arch-photogramm-remote-sens-spatial-inf-sci.net/XLVIII-4-W1-2022/27/2022/>.

Auflič, M. J., Herrera, G., Mateos, R. M., Poyiadji, E., Quental, L., Severine, B., Peternel, T., Podolszki, L., Calcaterra, S.,

Kociu, A., Warmuz, B., Jelének, J., Hadjicharalambous, K., Becher, G. P., Dashwood, C., Ondrus, P., Minkevičius, V., Todorović, S., Møller, J. J., Marturia, J., 2023. Landslide monitoring techniques in the Geological Surveys of Europe. *Landslides*, 20(5), 951–965. <https://doi.org/10.1007/s10346-022-02007-1>.

Baum, R. L., Godt, J. W., Savage, W. Z., 2010. Estimating the timing and location of shallow rainfall-induced landslides using a model for transient, unsaturated infiltration. *Journal of Geophysical Research: Earth Surface*, 115(F3). <https://doi.org/10.1029/2009JF001321>.

Bradski, G., 2000. The OpenCV Library. *Dr. Dobb's Journal of Software Tools*.

Carlà, T., Gigli, G., Lombardi, L., Nocentini, M., Casagli, N., 2021. Monitoring and analysis of the exceptional displacements affecting debris at the top of a highly disaggregated rockslide. *Engineering Geology*, 294, 106345. <https://doi.org/10.1016/j.enggeo.2021.106345>.

Casagli, N., Intrieri, E., Tofani, V., Gigli, G., Raspini, F., 2023. Landslide detection, monitoring and prediction with remote-sensing techniques. *Nature Reviews Earth & Environment*, 4(11), 51–64. <https://www.nature.com/articles/s43017-022-00373-x>.

Del Ventisette, C., Casagli, N., Fortuny-Guasch, J., Tarchi, D., 2012. Ruinon landslide (Valfurva, Italy) activity in relation to rainfall by means of GBInSAR monitoring. *Landslides*, 9(4), 497–509. <https://doi.org/10.1007/s10346-011-0307-3>.

Hermle, D., Gaeta, M., Krautblatter, M., Mazzanti, P., Keuschnig, M., 2022. Performance Testing of Optical Flow Time Series Analyses Based on a Fast, High-Alpine Landslide. *Remote Sensing*, 14(3), 455. <https://www.mdpi.com/2072-4292/14/3/455>.

Hermle, D., Keuschnig, M., Hartmeyer, I., Delleske, R., Krautblatter, M., 2021. Timely prediction potential of landslide early warning systems with multispectral remote sensing: a conceptual approach tested in the Sattelkar, Austria. 21, 2753–2772. <https://nhess.copernicus.org/articles/21/2753/2021/>.

Hojat, A., Arosio, D., Ivanov, V. I., Longoni, L., Papini, M., Scaioni, M., Tresoldi, G., Zanzi, L., 2019. Geoelectrical characterization and monitoring of slopes on a rainfall-triggered landslide simulator. *Journal of Applied Geophysics*, 170, 103844. <https://doi.org/10.1016/j.jappgeo.2019.103844>.

Horn, B. K., Schunck, B. G., 1981. Determining optical flow. 17, 185–203. [https://doi.org/10.1016/0004-3702\(81\)90024-2](https://doi.org/10.1016/0004-3702(81)90024-2).

Ivanov, V., Arosio, D., Tresoldi, G., Hojat, A., Zanzi, L., Papini, M., Longoni, L., 2020. Investigation on the role of water for the stability of shallow landslides—Insights from experimental tests. *Water*, 12(4), 1203. <https://www.mdpi.com/2073-4441/12/4/1203>.

Ivanov, V., Longoni, L., Ferrario, M., Brunero, M., Arosio, D., Papini, M., 2021. Applicability of an interferometric optical fibre sensor for shallow landslide monitoring—Experimental tests. *Engineering Geology*, 288, 106128. <https://doi.org/10.1016/j.enggeo.2021.106128>.

Kandelous, M. M., Moradi, B. A., Hopmans, J. W., 2015. An alternative tensiometer design for deep vadose zone monitoring. *Soil Science Society of America Journal*, 79(5), 1293–1296. <https://doi.org/10.2136/sssaj2015.03.0121>.

- Kollnig, H., Nagel, H. H., Otte, M., 1994. Association of motion verbs with vehicle movements extracted from dense optical flow fields. J.-O. Eklundh (ed.), *Computer Vision — ECCV '94*, Lecture Notes in Computer Science, Springer, Berlin, Heidelberg, 338–347.
- Lenzano, M., Lannutti, E., Toth, C., Rivera, A., Lenzo, L., 2018. Detecting Glacier Surface Motion by Optical Flow. 84, 33–42.
- Lissak, C., Bartsch, A., De Michele, M., Gomez, C., Maquaire, O., Raucoules, D., Roulland, T., 2020. Remote Sensing for Assessing Landslides and Associated Hazards. *Surveys in Geophysics*, 41(6), 1391–1435. <https://doi.org/10.1007/s10712-020-09609-1>.
- Longoni, L., Ivanov, V., Ferrario, M., Brunero, M., Papini, M., Arosio, D., 2022. Laboratory tests with interferometric optical fibre sensors to monitor shallow landslides triggered by rainfalls. *Landslides*, 19(3), 761–772. <https://link.springer.com/article/10.1007/s10346-021-01803-5>.
- Lucas, B. D., Kanade, T. et al., 1981. *An iterative image registration technique with an application to stereo vision*. 81, Vancouver.
- Mazzanti, P., Caporossi, P., Muzi, R., 2020. Sliding Time Master Digital Image Correlation Analyses of CubeSat Images for landslide Monitoring: The Rattlesnake Hills Landslide (USA). *Remote Sensing*, 12(44), 592. <https://www.mdpi.com/2072-4292/12/4/592>.
- Muhammad, M., Williams-Jones, G., Stead, D., Tortini, R., Falorni, G., Donati, D., 2022. Applications of Image-Based Computer Vision for Remote Surveillance of Slope Instability. *Frontiers in Earth Science*, 10. <https://www.frontiersin.org/articles/10.3389/feart.2022.909078>.
- Pantilie, C. D., Bota, S., Haller, I., Nedevschi, S., 2010. Real-time obstacle detection using dense stereo vision and dense optical flow. *Proceedings of the 2010 IEEE 6th International Conference on Intelligent Computer Communication and Processing*, 191–196.
- Panzeri, L., Mondani, M., Taddia, G., Papini, M., Longoni, L., 2022. ANALYSIS OF SNOWMELT AS A TRIGGERING FACTOR FOR SHALLOW LANDSLIDE. *International Multidisciplinary Scientific GeoConference: SGEM*, 22(1.1), 77–83. <https://www.proquest.com/docview/2781736481?pq-origsite=gscholar&fromopenview=true>.
- Scaioni, M., Crippa, J., Yordanov, V., Longoni, L., Ivanov, V., Papini, M., 2018. Some tools to support teaching photogrammetry for slope stability assessment and monitoring. 42, 453–460. <https://doi.org/10.5194/isprs-archives-XLII-3-W4-453-2018>.
- Vogel, C., Bauder, A., Schindler, K., 2012. OPTICAL FLOW FOR GLACIER MOTION ESTIMATION. *ISPRS Annals of the Photogrammetry, Remote Sensing and Spatial Information Sciences*, 1–3, 359–364. <https://www.isprs-ann-photogramm-remote-sens-spatial-inf-sci.net/I-3/359/2012/>.
- Walt, S. v. d., Schönberger, J. L., Nunez-Iglesias, J., Boulogne, F., Warner, J. D., Yager, N., Goullart, E., Yu, T., 2014. scikit-image: image processing in Python. *PeerJ*, 2, e453. <https://peerj.com/articles/453>.
- Wu, L., Huang, R., Xu, Q., Zhang, L., Li, H., 2015. Analysis of physical testing of rainfall-induced soil slope failures. *Environmental earth sciences*, 73, 8519–8531. <https://link.springer.com/article/10.1007/s12665-014-4009-8>.
- Yordanov, V., Truong, Q. X., Brovelli, M. A., 2023. Estimating Landslide Surface Displacement by Combining Low-Cost UAV Setup, Topographic Visualization and Computer Vision Techniques. *Drones*, 7(2), 85. <https://www.mdpi.com/2504-446X/7/2/85>.